The Astrophysical Journal, 747:136 (12pp), 2012 March 10 doi:10.1088/0004-637X/747/2/136

ON THE NATURE OF THE TRANSITION DISK AROUND LkCa 15

Andrea Isella, Laura M. Pérez, and John M. Carpenter
Department of Astronomy, California Institute of Technology, MC 249-17, Pasadena, CA 91125, USA; isella@astro.caltech.edu
Received 2011 September 19; accepted 2011 December 22; published 2012 February 23

ABSTRACT

We present Combined Array for Research in Millimeter-wave Astronomy 1.3 mm continuum observations of the T Tauri star LkCa 15, which resolve the circumstellar dust continuum emission on angular scales between 0.″2 and 3″, corresponding to 28–420 AU at the distance of the star. The observations resolve the inner gap in the dust emission and reveal an asymmetric dust distribution in the outer disk. By comparing the observations with theoretical disk models, we calculate that 90% of the dust emission arises from an azimuthally symmetric ring that contains about $5 \times 10^{-4}\ M_{\odot}$ of dust. A low surface-brightness tail that extends to the northwest out to a radius of about 300 AU contains the remaining 10% of the observed continuum emission. The ring is modeled with a rather flat surface density profile between 40 and 120 AU, while the inner cavity is consistent with either a sharp drop of the 1.3 mm dust optical depth at about 42 AU or a smooth inward decrease between 3 and 85 AU. We show that early science Atacama Large Millimeter Array observations will be able to disentangle these two scenarios. Within 40 AU, the observations constrain the amount of dust between 10^{-6} and 7 Earth masses, where the minimum and maximum limits are set by the near-infrared spectral energy distribution modeling and by the millimeter-wave observations of the dust emission, respectively. In addition, we confirm the discrepancy in the outer disk radius inferred from the dust and gas, which corresponds to 150 AU and 900 AU, respectively. We cannot reconcile this difference by adopting an exponentially tapered surface density profile as suggested for other systems, but we instead suggest that the gas surface density in the outer disk decreases less steeply than that predicted by model fits to the dust continuum emission. The lack of continuum emission at radii larger than 120 AU suggests a drop of at least a factor of five in the dust-to-gas ratio or in the dust opacity. We show that a sharp dust opacity drop of this magnitude is consistent with a radial variation of the grain size distribution as predicted by existing grain growth models.

Key words: instrumentation: interferometers – planet–disk interactions – protoplanetary disks – stars: low-mass – stars: pre-main sequence – techniques: high angular resolution

Online-only material: color figures

1. INTRODUCTION

Over the past decade, the *Spitzer Space Telescope* has identified an increasing population of circumstellar disks surrounding pre-main-sequence stars that display a deficit of near- and mid-infrared flux compared to a "classical" T Tauri star, while exhibiting similar levels of far-infrared emission. The spectral energy distribution (SED) of these objects suggests that these stars lack warm dust in the inner disks regions, while substantial emission at longer wavelengths indicates that the outer disk remains quite massive (see, e.g., Calvet et al. 2005). These so-called transition disks may be intermediate systems between young (∼1–10 Myr), optically thick, gas rich protoplanetary disks and old (>10 Myr), optically thin, gas poor, debris disks, where significant disk evolution has occurred and a planetary system might have formed.

Subsequent high-resolution images of the optically thin millimeter-wave dust emission confirm the SED modeling predictions that the inner disk in transition disks is depleted of dust (Andrews et al. 2011b; Brown et al. 2009; Hughes et al. 2009; Piétu et al. 2006). However, spatially resolved observations of the gas emission show that some of these dust depleted cavities contain a significant amount of gas (Piétu et al. 2007) and that the size of the hole is not always consistent with SED modeling (Andrews et al. 2011b). Furthermore, recent high-angular-resolution observations of the mm-wave dust emission have also revealed that some "classical" disks have dust depleted inner regions similar to those of "transition" disks, but do not show any deficit in the infrared excess (Isella et al. 2010a, 2010b; Andrews et al. 2011b). These results demonstrate that SEDs alone cannot provide a complete picture of the disk structure. High-angular-resolution millimeter-wave observations are essential to remove some of the degeneracies that limit SED modeling, and therefore provide a more accurate description of the radial distribution of circumstellar material.

To determine the physical phenomena responsible for disk cavities, measurements of the mass surface density profile $\Sigma(r)$ are essential. To first order, circumstellar disks evolve via viscous spreading, where friction forces redistribute the material and smoothly shape the disk surface density (Lynden-Bell & Pringle 1974). Disk photoevaporation by energetic photons might reduce the amount of disk material. Models that combine these two processes have been the focus of many theoretical studies (Alexander et al. 2006a, 2006b; Gorti et al. 2009; Owen et al. 2010). These models suggest that viscous evolution proceeds unperturbed by photoevaporation until the mass accretion rate throughout the disk is comparable with the photoevaporation rate. After this phase, which can last for a few Myr for typical values of the stellar radiation and disk surface density, a gap opens at a few AU from the central star, where the photoevaporation rate is the largest. The material within the gap then drains quickly onto the central star leaving a gas-free cavity in the disk. Although the exact timescale for the formation of the cavity varies between different models, they all predict an order of magnitude drop in the gas surface density over a 1 AU radial extent at the edge of the cavity.

Alternatively, cavities in the disk can be produced by the gravitational interaction between giant planets and the disk

material (see, e.g., Bryden et al. 1999). Although this is a common explanation for transition disks, Zhu et al. (2011) have shown that even multiple giant planets cannot account for optically thin cavities larger than 20 AU, unless the small grains within the region perturbed by the planets are efficiently removed. Similarly to the photoevaporation model, the planet–disk interaction predict a sharp drop of the dusty and gas density at the edge of the region cleared by the planet tidal interaction.

A third possible origin of the inner disk cavities is that the dust grains have grown from micron-sized particles to centimeter-sized pebbles. Therefore, the cavities reflect a reduced dust opacity and not a reduced matter density. Theory predicts that dust coagulation is more efficient in the dense inner disk (Tanaka et al. 2005; Dullemond & Dominik 2005) and as the dust particles grow, the opacity of the dust diminishes. Current models of grain growth anticipate a continuous radial variation of the dust opacity within the disk (e.g., Birnstiel et al. 2010), whose observational signature corresponds to a gradual transition between the inner and outer disk structure.

Among the known stars with a transition disk, the 2–5 Myr old star LkCa 15 represents an outstanding case. LkCa 15 is a K5 star ($L_\star = 0.74\ L_\odot$, $M_\star = 1.0\ M_\odot$; Simon et al. 2000; Kenyon & Hartmann 1995) located in the Taurus star-forming region at a distance of about 140 pc (van den Ancker et al. 1998). Its disk is characterized by a partially dust-depleted inner region of about 50 AU in radius (Andrews et al. 2011b; Espaillat et al. 2007; Piétu et al. 2006) and a mass accretion rate of about $3 \times 10^{-9}\ M_\odot\ \mathrm{yr}^{-1}$ (Hartmann et al. 1998). The disk SED is characterized by the presence of an infrared excess over the stellar photosphere, which can be explained by the presence of hot dust within a few AU from the central star (Espaillat et al. 2007; Mulders et al. 2010). The disk has a very active chemistry observed in several molecular transitions (Chapillon et al. 2008; Piétu et al. 2007; Öberg et al. 2010) and also exhibits Keplerian rotation out to a radius of 900 AU (Piétu et al. 2007). These latter observations suggest that gas is present at an orbital radius as small as 10 AU, and therefore well within the cavity observed in the dust continuum emission. Ground-based H-band (1.6 μm) observations reveal the presence of an elliptical structure in correspondence to the edge of the dust inner cavity (Thalmann et al. 2010). Finally, Kraus & Ireland (2012) have recently reported the discovery through aperture masking of a possible 6 M_J mass protoplanet located inside the continuum cavity at an orbital distance of 16 AU from the central star. These observations suggest that the cavity might be indeed shaped by the dynamical interaction with a giant planet. However, Zhu et al. (2011) and Dodson-Robinson & Salyk (2011) have argued that a cavity 50 AU in radius cannot be explained by a single planet, and that additional giant planets or clearing mechanisms are required to explain these observations.

In this paper we present new observations of the 1.3 mm dust thermal emission obtained with the Combined Array for Research in Millimeter-wave Astronomy (CARMA). The observations achieve an angular resolution of 0.″2 corresponding to a spatial scale of 28 AU at the distance of star, which is a factor of two improvement with respect of existing observation of this system. In Sections 2 and 3 we present our observations of LkCa 15 and discuss the morphology of the dust emission. The method used to analyze the data is discussed in Section 4, and the results are presented in Section 5. In Section 6 we discuss the possible origin of the dust continuum cavity and of the whole disk structure. A summary of the main results follows in Section 7.

2. OBSERVATIONS AND DATA REDUCTION

LkCa 15 was observed with CARMA array configurations A, B, C, and E, providing projected baseline lengths between 6 and 1700 m. C-configuration observations were obtained in 2007 October and are discussed in Isella et al. (2009). Observations in B configuration were obtained in 2008 December. The receivers were tuned at a local oscillator (LO) frequency of 224.75 GHz and the continuum emission was observed using three contiguous bands of 468 MHz each in both correlator side bands, resulting in a total bandwidth of about 3 GHz. Flux and pass band calibration were derived by observing Uranus and 3C84, respectively; 0510+180 was observed every 15 minutes to derive the atmospheric and instrumental phase corrections. A- and E-configuration observations were carried out in 2010 November and 2011 January, respectively, using the upgraded CARMA correlator which provides a maximum continuum bandwidth of about 8 GHz. The receivers were tuned to the same LO frequency used for C- and B-configuration observations. The upper and lower correlator side bands were configured with eight partially overlapping bands of 494 MHz each in order to cover the full bandwidth. The band pass shape was calibrated by observing 3C84 and 3C454.3; flux calibration was set by observing Uranus and cross checked using almost simultaneous observations of 3C84 and 3C454.3 obtained with the Sub-Millimeter Array (SMA) at the frequency of 225 GHz. The estimated uncertainty in the absolute flux calibration is 10%. Atmospheric and instrumental effects were corrected by observing the nearby quasar 0510+180 every 6–10 minutes, depending on the array configuration.

The data taken in the four different array configurations were independently calibrated using the MIRIAD software package. The data set were shifted both in right ascension and declination to compensate for the stellar proper motion (see the Appendix) and combined to increase the image sensitivity and dynamic range. Images were then obtained through standard inversion of the uv data using different weighting functions to emphasize the morphology of the dust emission on both large and small angular scales. The images were deconvolved using the CLEAN algorithm.

3. MORPHOLOGY OF THE CONTINUUM EMISSION

The high dynamic range obtained by combining the compact and extended array configurations enables CARMA to reveal the structure of the dust emission on both small and large angular scales. Figure 1 shows the map obtained by adopting three different weighting functions to achieve an angular resolution of (a) 3.″0 × 2.″6 (b) 1.″1 × 0.″5 and (c) 0.″21 × 0.″19. In panel (a), the disk emission appears fairly symmetric and centered near the position of the star. The integrated flux measured in a circular aperture of 4″ in radius, is 128 ± 5 mJy, and it is consistent with the value measured by Piétu et al. (2006). In panel (b), the emission has two peaks separated by about 0.″3. In addition, the low intensity contours show that the disk extends toward the northwest. The integrated flux, as measured in a circular aperture of 2″ in radius is 127 ± 15 mJy, where the uncertainty accounts only for random noise. Finally, the map shown in panel (c) reveals that the dust emission comes from an elliptical ring that extends for about 1.″8 along its major axis, and for about 1.″2 in the perpendicular direction. Assuming that the emission arises from a circular disk, the aspect ratio of the contour levels leads to a disk inclination of about 50°, a position angle measured east from north of about 60°, and a disk diameter

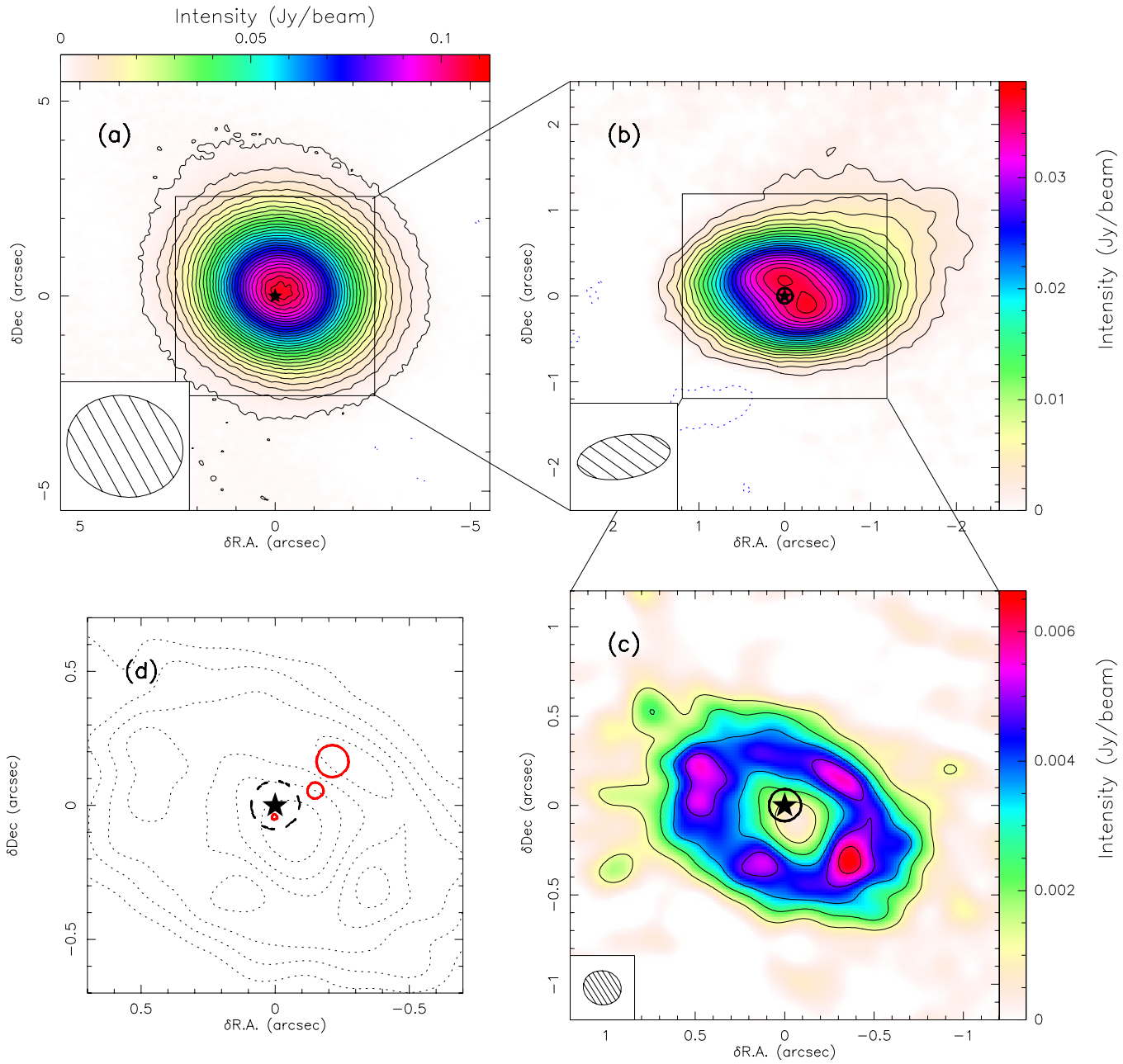

Figure 1. Maps of the 1.3 mm dust continuum emission observed toward LkCa 15 employing three different weighting schemes of the *uv* data. (a) Natural weighting was adopted to achieve an FWHM beam size of 3.″0 × 2.″6. Intensity contours start at 3σ and are spaced by 6σ, where the 1σ noise level is 0.58 mJy beam^{-1}. (b) Robust weighting was adopted to achieve a resolution of 1.″1 × 0.″5. Contours are plotted every 3σ, where the 1σ noise level is 0.53 mJy beam^{-1}. (c) Uniform weighting was adopted to achieve an FWHM beam size of 0.″21 × 0.″19. Contours are plotted every 3σ, where the 1σ noise level is 0.43 mJy beam^{-1}. (d) The large, medium, and small red circles show the position of the center of symmetry of the dust emission corresponding to panels (a), (b), and (c), respectively. The symbol ⋆ marks the position of the star and the surrounding circle its uncertainty, calculated as discussed in the Appendix. The dotted curves show the intensity contours as in panel (c).

(A color version of this figure is available in the online journal.)

of about 250 AU for the stellar distance of 140 pc. The total integrated flux measured in an elliptical aperture with major axis of 2.″4 and the same aspect ratio of the disk is 117 ± 10 mJy. CARMA observations reveal for the first time an asymmetric dust distribution in LkCa 15 outer disk, while the ring-like structure presented in panel (c) of Figure 1 is consistent with earlier lower angular resolution observations of LkCa15 (Piétu et al. 2006; Andrews et al. 2011b).

To investigate the properties of the dust emission we define the center of symmetry (x_c, y_c) of the map intensity $I(x, y)$ such that $x_c = \Sigma x I/\Sigma I$ and $y_c = \Sigma y I/\Sigma I$, where the sum extends over all positions brighter than five times the noise level in the image. Since $I(x,y)$ depends on the weighting scheme adopted in the image formation process, the position of the center of the emission is a function of the angular resolution in the image. Panel (d) in Figure 1 shows the center of symmetry for the three maps discussed above. The stellar position and its uncertainty, as expected from proper motion correction (the Appendix), are shown by the star symbol and the surrounding circle, respectively. We find that the center of symmetry of the highest

angular resolution map is consistent with the position of the star, and both appear to be shifted by about 0.″1 with respect to the center of innermost intensity contours levels. Although the astrometric uncertainty on the position of the star does not allow us to firmly conclude on the nature of this shift, we note that a pericenter offset of similar magnitude (0.″064) and direction has been recently derived from infrared observations by Thalmann et al. (2010).

At lower angular resolution the center of symmetry moves progressively toward the northwest up to a distance of about 0.″3 from the star. This shift of the center of symmetry, which results from the asymmetry observed at intermediate angular resolution, suggests that the outermost disk regions might have been perturbed. However, about 90% of the dust emission arises from the fairly symmetric ring shown in panel (c). The structure of this ring and the significance of the observed asymmetries are discussed in the following two sections.

4. DISK MODEL

The disk properties were inferred using two prescriptions for the disk surface density.

The first is a classical power law $\Sigma(r) = \Sigma_0(r_0/r)^p$ characterized by four free parameters: the inner radius $r_{\rm in}$, the outer radius $r_{\rm out}$, the normalization value Σ_0, and the slope p. This parameterization provides the simplest form for the disk surface density that mimics the sharp inner disk truncation caused by disk photoevaporation or by dynamical interaction with a giant planet, but has the disadvantage of introducing an unphysical sharp edge of $\Sigma(r)$ at the disk outer radius.

To obtain a smoother form of $\Sigma(r)$ we adopt a second parameterization given by the similarity solution for the disk surface density of a viscous Keplerian disk (see Lynden-Bell & Pringle 1974; Hartmann et al. 1998), adopting the form presented in Isella et al. (2009),

$$\Sigma(r) = \Sigma_t \left(\frac{r_t}{r}\right)^{\gamma} \times \exp\left\{-\frac{1}{2(2-\gamma)}\left[\left(\frac{r}{r_t}\right)^{(2-\gamma)} - 1\right]\right\}. \quad (1)$$

This functional form has five free parameters, i.e., the disk inner and outer radius ($r_{\rm in}$ and $r_{\rm out}$), the characteristic radius r_t, the normalization value $\Sigma_t = \Sigma(r_t)$, and the slope γ, which is related to the radial viscosity profile through the equation $\nu(r) \propto r^{-\gamma}$.

Since the limited angular resolution and sensitivity of existing observations does not generally allow to fit for all five parameters, previous studies of the dust distribution in transitional disks based on this form of the surface density adopted two different approaches. In Isella et al. (2009, 2010a, 2010b), we fixed the disk inner radius at the dust evaporation radius (<0.5 AU), and compared the model to the observations to constrain the values of γ, r_t, and Σ_t. In this way, we found that the cavities in the dust continuum emission observed in LkCa 15, RY Tau, and MWC 758 disks might be explained with small inner disk radii and negative values of γ, which leads to a smoothly increasing surface density up to a radius $r_{\rm max} = r_t \times (-2\gamma)^{1/(2-\gamma)}$. A different approach was adopted by Andrews et al. (2011b), who fixed the slope $\gamma = 1$, and derived the disk inner radius $r_{\rm in}$, r_t, and Σ_t.[1]

The first modeling procedure, i.e., variable γ and fixed $r_{\rm in}$, stems from the idea that transitional disks might be shaped a global physical process, such as the disk viscosity and/or the variation of the dust opacity due to the grain growth. By contrast, the second case assumes that the disk surface density profile follows the α-constant prescription of the viscosity (Shakura & Sunyaev 1973) which leads to $\gamma = 1$, and that the cavities observed in the dust emission results from the inner truncation of the disk, perhaps due to planets, which does not effect the density distribution at larger radii. In order to investigate the nature of LkCa 15 disk we here adopt both approaches which we will be referred to as *smooth* and *truncated* viscous models.

The radiation transfer equation within the disk is solved by adopting the "two-layer" approximation of Chiang & Goldreich (1997), in which the disk is described through a warm surface layer and a cooler midplane interior. Both temperatures are calculated as a function of the orbital radius by iterating on the vertical disk structure (see Dullemond et al. 2001). The disk is in hydrostatic equilibrium between the gas pressure and the stellar gravity, which leads to a flared geometry with the opening angle increasing with the distance from the central star. Because a flared disk geometry tends to over predict the far-IR disk emission in LkCa 15, we allow the disk scale height H_p to be lower than the self-consistent solution $\tilde{H}_p$ by introducing a settling parameter $\Psi < 1$, so that $H_p = \Psi\tilde{H}_p$. Following Mulders et al. (2010) and Espaillat et al. (2007), we chose $\Psi = 0.3$.

The dust opacity is calculated by assuming an interstellar grain composition (Pollack et al. 1994) and a particle size distribution between a minimum ($a_{\rm min}$) and a maximum ($a_{\rm max}$) size according to $n(a) \propto a^{-q}$. The spectral slope of the LkCa15 mm-wave disk emission is $\alpha = 3.4$, as computed from the observed flux density at 1.3 mm (128 mJy; see Section 2) and 7 mm (0.44 mJy; Rodmann et al. 2006). Assuming that the emission at these wavelengths is optically thin and follows the Rayleigh–Jeans approximation, this implies a dust opacity slope $\beta = 2-\alpha = 1.4$, which is reproduced adopting $a_{\rm min} = 0.5\,\mu$m, $a_{\rm max} = 0.5$ mm, and $q = 3.5$. For sake of simplicity we assume that the dust opacity is constant throughout the disk.

From the derived dust density, temperature, and opacity we calculate the disk SED and synthetic disk images in the dust continuum at 1.3 mm. We assume that the center of the disk corresponds to the center of symmetry of the dust emission shown in panel (c) of Figure 1. The synthetic disk images are then Fourier transformed and sampled at the positions on the (u, v) plane corresponding to the CARMA observations. Best-fit values for the free parameters that define the disk surface density, and for the disk inclination and position angle are then derived through a χ^2 minimization based on a Markov Chain Monte Carlo simulation as discussed in Isella et al. (2009).

5. RESULTS

5.1. Constraints on the Disk Surface Density

The best-fit parameters for both the smooth and the truncated disk models are listed in Table 1. The quoted uncertainties correspond to the 68.3% confidence level and were calculated by integrating the marginalized probability distribution resulting from the Monte Carlo fitting procedure (see Appendix A of Isella et al. 2009). In addition to the free model parameters, we list within the square brackets some relevant values for the disk structure, such as the inner and outer disk radius for the smooth viscous model, the outer radius and γ for the viscous truncated disk model, and the normalization radius for the power-law model. Finally, the last column of the table shows the total

[1] Andrews et al. (2011b) adopt a different parameterization of the similarity solution for the surface density, which depends on the characteristic radius $r_c = r_t \times [2(2-\gamma)]^{1/(2-\gamma)}$ and on the normalization value $\Sigma_c = \Sigma_t \times [2(2-\gamma)]^{\gamma/(\gamma-2)}$.

Table 1
Best-fit Parameters for the Smooth and Truncated Models

Model	Incl.	PA	$r_{\rm in}$	r_t	$r_{\rm out}$	γ	Σ_t	M_d
Smooth viscous	$50.5^{+0.9}_{-0.9}$	$64.4^{+1.5}_{-1.5}$	[0.2]	$60.2^{+0.6}_{-0.8}$	[160]	$-2.15^{+0.08}_{-0.10}$	$10.37^{+0.20}_{-0.24}$	[0.06]
Truncated viscous	$52^{+1.0}_{-1.2}$	$67^{+1.6}_{-1.6}$	$52^{+1.3}_{-2.0}$	$20^{+1.2}_{-1.0}$	[190]	[1]	270^{+20}_{-15}	[0.1]
Model	Incl.	PA	$r_{\rm in}$	r_0	$r_{\rm out}$	p	Σ_0	M_d
Power-law	$50.7^{+1.2}_{-1.0}$	$63.5^{+1.8}_{-1.2}$	$42.5^{+2.4}_{-1.2}$	[60]	$119.7^{+1.4}_{-2}$	$0.72^{+0.14}_{-0.28}$	$9.92^{+1.1}_{-0.64}$	[0.05]

Notes. The numbers in square brackets are either fixed values (i.e., the normalization radius r_0) or the result of the model fitting. The inclination and position angle are expressed in degrees, the radii $r_{\rm in}$, $r_{\rm out}$, r_t, and r_0 in AU, the disk surface densities Σ_t and Σ_0 in g cm^{-2}, and the disk mass M_d in solar masses.

disk mass. In addition to the statistical errors, the surface density Σ_t and the total disk mass M_d are affected by systematic errors due to the flux calibration and to the uncertainty on the dust opacity. We estimate a 10% uncertainty from flux calibration based upon CARMA flux calibration monitor programs. The uncertainty on the dust opacity is more difficult to quantify and might vary between 5% and 20% once the slope of the millimeter SED is used to constrain the grain size distribution (see the discussion in Isella et al. 2009, 2010a).

Figure 2 presents the comparison between the best-fit models and observations. Panel (a) shows the real part of the observed correlated flux (points with error bars), the visibility profile of the best-fit model (solid line), and the residuals obtained by subtracting the model visibility to the observations. Panels (b) and (c) show the maps of the residuals obtained adopting the same weighting functions and color scale of panels (b) and (c) of Figure 1, respectively. Finally, the surface density profiles corresponding to the best-fit models are shown in Figure 3, along with the corresponding uncertainties.

We find that the smooth viscous and the power-law models provide acceptable fits to the observations. The first model is characterized by $\gamma = -2.15$, which is more negative, although consistent within the uncertainties, with the γ value derived in 2009 by fitting only the smaller spatial frequencies. Both models suggest a disk inclination of $51^\circ \pm 1^\circ$ and a position angle of $64^\circ \pm 2^\circ$, that agrees with the values derived by Andrews et al. (2011b). By contrast, the truncated viscous model characterized by $\gamma = 1$ does a worse job in reproducing the structure of the dust emission and leads to significative residuals both inside the continuum cavity and along the dusty ring (second row of Figure 2). The comparison between the best-fit surface densities (Figure 3) shows that the first two models are characterized by rather flat density profiles between about 50 and 120 AU, while the truncated viscous model produces a much steeper decrease in the surface density in this radial range. This result therefore implies that the surface density in LkCa 15 disk is inconsistent with the α-constant prescription at least in the radial range probed by our observations.

The power-law and the smooth viscous models reproduce equally well the ring observed in the dust emission. To understand why our observations cannot disentangle these two models, we show in Figure 4 the difference between the correlated flux of the power-law and the smooth viscous model as a function of the spatial frequency (solid curve), along with the 1σ and 2σ noise level provided by our observations (blue and red boxes, respectively). The maximum difference between the two models is about 6 mJy at 580 kλ and is within the 2σ noise level. The figure also shows that our ability to disentangle different surface density profiles is not hampered by the angular resolution (i.e., by the maximum spatial frequency achieved by our observations), but by the noise level on spatial frequencies between 100 kλ and 700 kλ where the difference between the two models is the greatest. This is an important point to consider in planning future observations and will be discussed further in Section 6.2.

Although we cannot achieve a model-independent constraint of the disk surface density, our observations provide an upper limit of the amount of small solid particles present in the LkCa15 inner disk. We find that the upper limit is set by the best-fit smooth viscous model, since any additional amount of dust in the inner disk provides a worse fit to the data. Integrating this density profile between 3 and 42 AU, we calculate a dust mass of 7 Earth masses ($M_\oplus$), or about 2 M_J of gas assuming a standard gas-to-dust ratio of 100. Additional constraints of the gas density come from spatially resolved observations of the ^{12}CO and ^{13}CO (2-1) line emission (Piétu et al. 2007). These observations are characterized by an angular resolution between $1''$ and $2''$, and were compared to power-law disk models to derive the gas density and temperature radial profile. Piétu et al. (2007) find that CO might be present down to a radius of 10 AU, and that a sharp truncation of the gaseous disk at 50 AU is excluded at the 7σ level. These observations also suggest the presence of about 2 M_J of gas within 42 AU from the central star. The amount of dust within 42 AU from the central star is also constrained by the infrared SED modeling, which is discussed in Section 5.3.

Finally, we confirm the discrepancy found by Piétu et al. (2007) between the disk outer radius inferred from the dust continuum emission, i.e., about 160 AU, and that derived from the observations of the molecular line emission, which, depending of the observed molecule, varies between 550 AU (^{13}CO) and 900 AU (^{12}CO). Gaseous disks are found systematically larger than dusty disks in almost all the objects observed at high angular resolution (Isella et al. 2007; Piétu et al. 2005, 2007). In some cases this discrepancy can be reconciled by adopting an exponentially tapered surface density profile, as the one resulting from the disk viscous evolution (Hughes et al. 2008; Isella et al. 2009). This model predicts that dust is present up to the outer radius inferred from the gas but the millimeter-wave dust emission coming from the outer disk is too low to be detected by existing observations. In the case of LkCa 15, we have used the gas emission model discussed in Isella et al. (2007) to calculate the ^{12}CO J = 2-1 emission corresponding to the smooth and truncated viscous best-fit models for the dust continuum emission. The ^{12}CO surface density is described by Equation (1), with γ and r_t as in Table 1, and assuming a CO/H2 abundance of 10^{-4}, as measured in the molecular clouds. By assuming that the ^{12}CO molecules are in thermal equilibrium with the dust, we find that the ^{12}CO emission should be confined within 300 AU and 550 AU from the central star for the smooth and truncated viscous model, respectively, despite the fact that the ^{12}CO

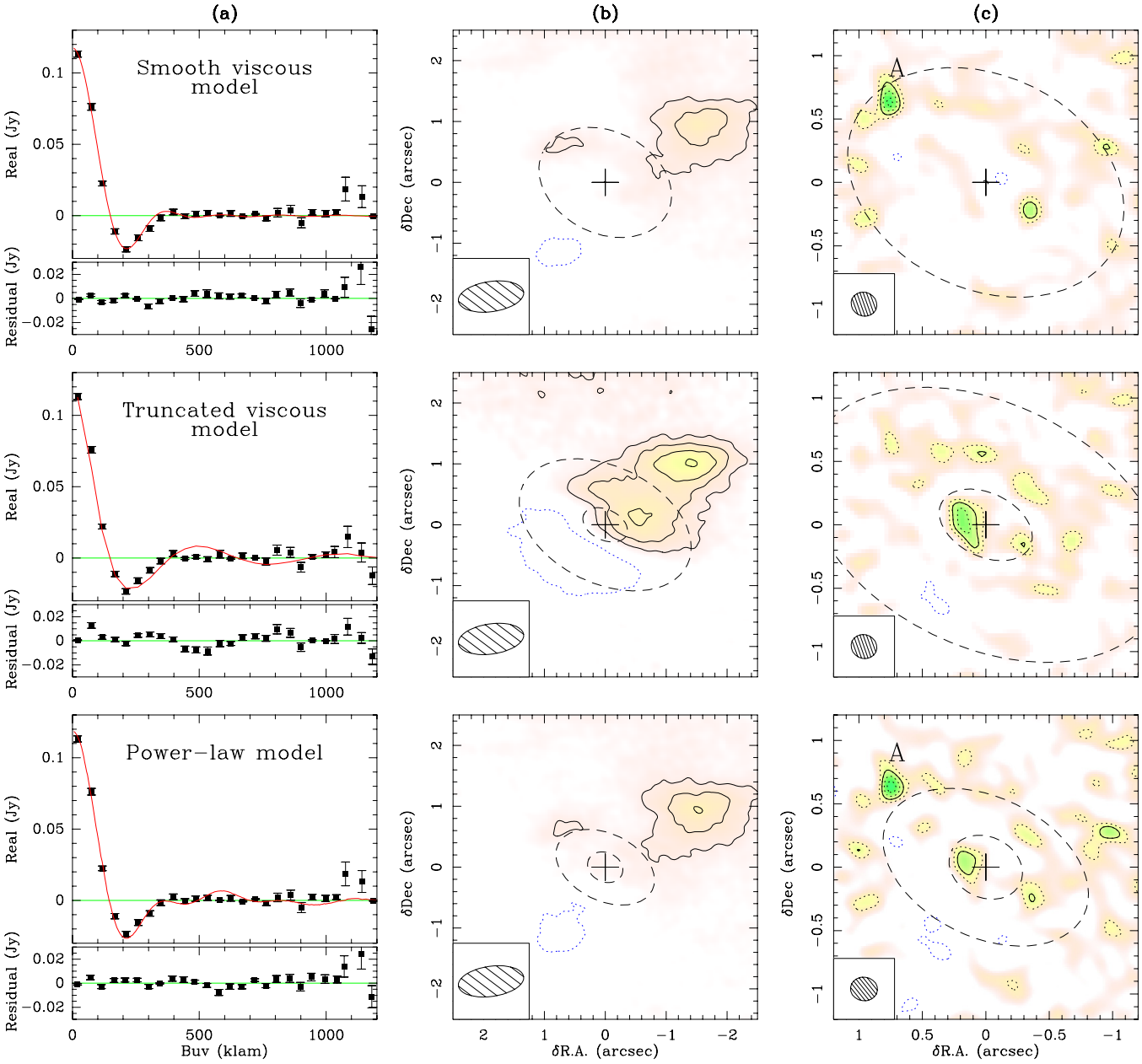

Figure 2. Comparison between the observations and the best-fit models calculated assuming a smooth viscous (top panels), a truncated viscous (middle panels), and a power-law (bottom panels) surface density profile. Panel (a) shows the real part of the correlated flux observed at 1.3 mm (square points with error bars), along with the best-fit model (solid line) and the residuals. To account for the disk geometry, the data have been deprojected using the values for the inclination and position angle listed in Table 1. Panels (b) and (c) show maps of the residuals obtained with the weighting functions used in panels (b) and (c) in Figure 1. The color scale, the map size, and noise level are also the same as in Figure 1. Solid contours are plotted every 3σ, while the dotted contours in panel (c) stars at 2σ and are spaced by 1σ. The dashes ellipses show the inner and outer disk radius corresponding of the best-fit models listed in Table 1.

(A color version of this figure is available in the online journal.)

density extends in practice to infinity. The fact that ^{12}CO is observed out to a radius of 900 AU suggests therefore that the exponential taper that characterizes the viscous surface density is not a good explanation for the different radial extent of the gas and dust emission in LkCa 15. Other possible explanations are discussed in Section 6.3.

5.2. Sub Structures and Asymmetries

Figure 2 shows the map of the residuals obtained by subtracting the best-fit models from the observations in the Fourier domain, and by adopting different weighting functions in the image reconstruction process. Panels (b) and (c) adopt the same weighting functions, use the same color scale, and have the same size of the maps shown in the panels (b) and (c) of Figure 1.

Panel (b) clearly shows the asymmetric emission in the northwest side of the disk discussed in Section 3. The integrated flux is about 8 mJy, which corresponds to a dust mass between 5 and 10 M_J for a dust temperature between 20 and 40 K.

As for the residuals along the dusty ring and inside the cavity, we discuss only the case of the smooth viscous and power-law model, since we have concluded in the previous section that the truncated viscous model does not provide as good of a fit to the observations. For these two models, the brightest residual in panel (c) is identified with the letter A and has peak flux of

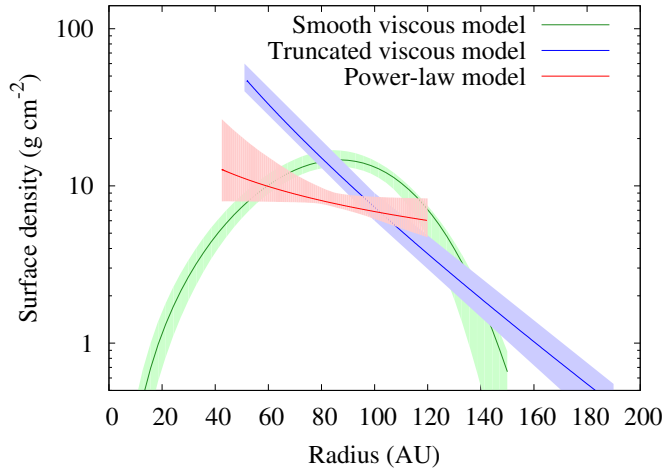

Figure 3. Surface density profiles corresponding to the smooth and truncated viscous best-fit models (green and blue, respectively), and to the power-law model (red). The colored regions represent the 3σ uncertainty interval.

(A color version of this figure is available in the online journal.)

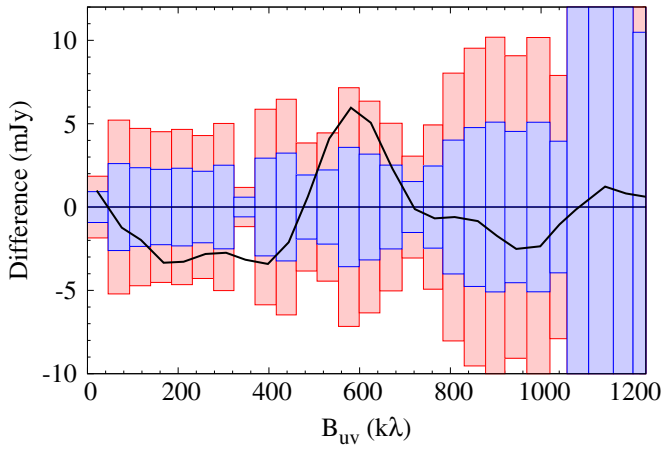

Figure 4. Difference between the 1.3 mm correlated fluxes (solid curve) of the best-fit power-law and smooth viscous models. The blue and red triangles show the 1σ and 2σ noise levels of the CARMA observations. The figure shows that the sensitivity of CARMA observations is not sufficient to distinguish between the two surface density parameterizations.

(A color version of this figure is available in the online journal.)

2.4 mJy. It is located along the major axis of the disk at the physical distance of 140 AU from the center, and therefore very close, or just outside, the outer disk radius inferred from our disk modeling, which is represented by the large dashed ellipses in Figure 2. At this distance from the central star, the dust is expected to have a temperature of about 40 K, which leads to a mass of dust of about 1.3 M_J.

The significance of this residual depends critically on knowing the value of the noise in our map and how it varies with the distance from the center due to the antenna primary beam attenuation. A theoretical value for the noise can be obtained from the weights on each visibility point, which are measured at the time of the observations and depends on the effective area of the telescope and the system temperature (see, e.g., Thompson et al. 1991). However, if the observed source is bright, this estimate does not take into account possible effects due to the image deconvolution, such as the presence of residual side lobes in the final map, and dynamic range limitations due to the atmospheric decorrelation (i.e., seeing) and calibration errors.

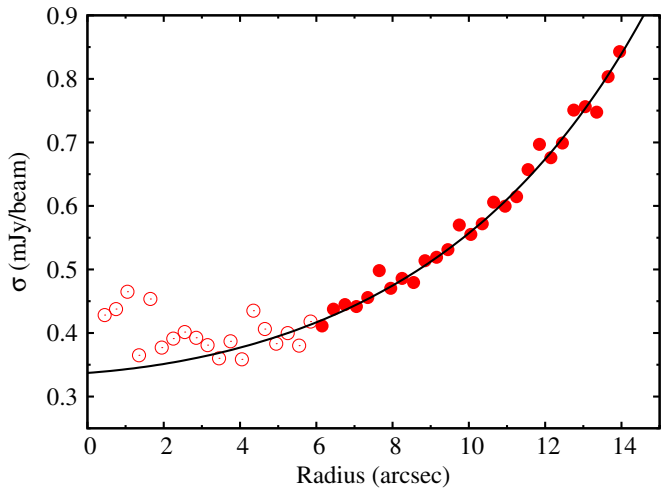

Figure 5. Radial variation of the noise in the map presented in panel (c) of Figure 2. The circles show the standard deviation (σ) of the intensity measured in concentric 0.″2 wide annuli. The filled circles correspond to annuli in which the intensity distribution is consistent with a standard normal distribution, as expected if the emission is due to Gaussian noise. The open circles indicate the radii where the intensity distribution is dominated by true emission. The solid curve represents the theoretical noise as computed from the weights on the visibility data.

(A color version of this figure is available in the online journal.)

We estimated the noise in the images as follow. We divide the intensity map in concentric annuli characterized by a width of 0.″2. For each annulus we calculate the mean intensity and the standard deviation σ. If the emission is due only to Gaussian noise, then the mean is 0 and the standard deviation of the intensity is equal to the noise. For each annulus, we check that the distribution is Gaussian by creating a histogram for the intensity and fitting a normal distribution. Otherwise, if the annulus contains true emission, the intensity distribution will deviate from the normal profile. In this case σ will give an upper estimate of the noise.

Figure 5 shows the radial variation of the standard deviation of the intensity, σ. At radii larger than 6″ (filled circles), the intensity distribution is well described by a standard normal function; σ increases with the radius as the inverse of the antenna primary beam profile and it is equal to the theoretical noise indicated by the solid curve. Within 6″, the intensity is a combination of Gaussian noise and true emission and its distribution deviates from the standard normal profile. In this region, the noise in the map may assume values between the theoretical noise and σ. This implies a noise upper limit of 0.47 mJy beam^{-1} at the position of the residual A (i.e., 1″), which leads to a signal-to-noise ratio of 5.1, given the measured peak flux of 2.4 mJy.

The significance level of residual A can be estimated by multiplying the normal probability corresponding to a 5.1σ residual (3.4×10^{-7}) by the number of independent pixels in our map. If each resolution element (0.″21 × 0.″19) is accounted as independent pixel, then the number of independent pixels within the 1.3 mm CARMA field of view (27″) is about 18000, and the probability that the residual might be due to random noise is smaller than 0.6%, or about 2.8σ. This result suggests that the residual might trace a real compact overdensity in the dust distribution with respect to the best-fit surface density profile, but more sensitive observations are required to investigate the nature of this emission.

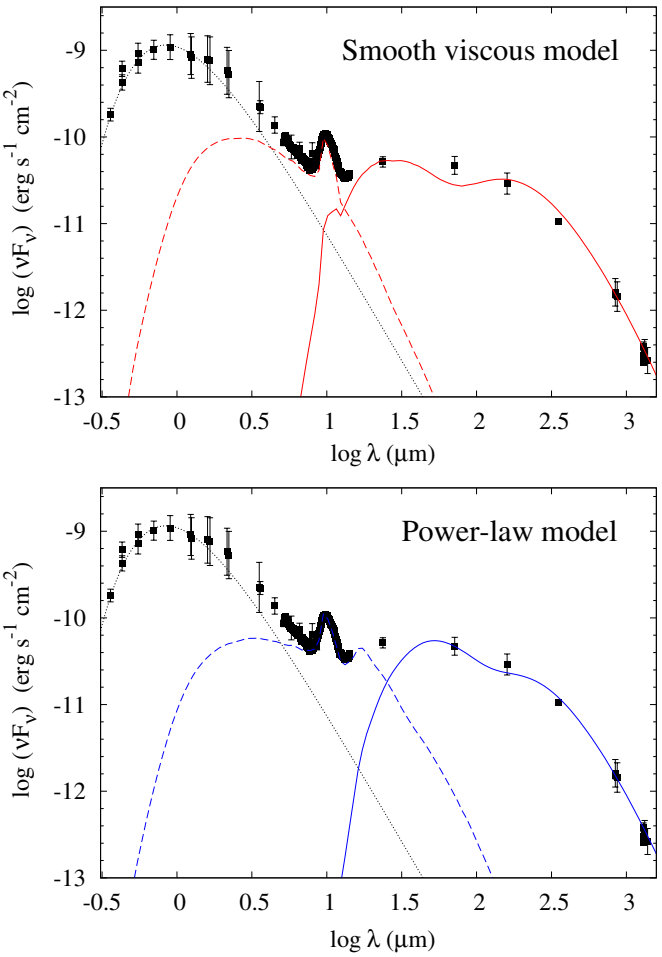

Figure 6. SED of LkCa 15. Filled squares present photometric data from the literature (Kenyon & Hartmann 1995; Hartmann et al. 2005; Espaillat et al. 2007; Rebull et al. 2010; Kitamura et al. 2002; Dutrey et al. 1996; Andrews & Williams 2005, 2007; Öberg et al. 2010) and from our new CARMA observations. Infrared photometry at 9 μm, 19.6 μm, and 90 μm is from the Akari archive, and the infrared spectrum from 5 to 14 μm is from archival *Spitzer* Infrared Spectrograph (IRS) observations. The solid curves show the SED of the best-fit models for the smooth (top panel) and the power-law (bottom panel) surface density parameterization. The dashed curves indicate the SED required to reproduce the observed near- and mid-infrared excess. As discussed in the text, this additional component can arise either from a narrow ring of optically thick dust or from a more extended optically thin region.

(A color version of this figure is available in the online journal.)

All the other residuals in panel (c) of Figure 2 have flux within ±4.5 times the noise level. The probability that any one of these residuals could originate from random noise is greater than 10%.

5.3. Understanding the SED

Figure 6 compares the observed SED for LkCa 15 with the SED inferred from the best-fit models to the millimeter data. Both the smooth viscous (upper panel) and the power-law (lower panel) provide a good agreement with the observations at millimeter wavelengths. At infrared wavelengths, the model SED strongly depends on the disk surface density profile. In the case of the smooth viscous model, the disk is optically thick to the stellar radiation starting from 3 AU, and the agreement with the observation extends to about 20 μm. At shorter wavelengths the model SED underestimates the observed emission from the disk. This is due to the fact that the surface density within a few AU from the central star is lower than 10^{-6} g cm^{-2} and the near-infrared disk emission is negligible with respect to the stellar photosphere. In the case of the power-law model, the predicted SED agrees with the observation only at wavelengths longer than 50 μm due to the cutoff of the dust density at 42.5 AU. Independently on the adopted model, the near-infrared emission observed toward LkCa 15 requires the presence of material with temperature between 1000 and 2000 K in excess of what predicted by our models.

For a power-law surface density profile truncated at 42.5 AU, the near infrared emission can be explained by two different models, as discussed in Mulders et al. (2010). In the first case, the emission comes from a small optically thick disk that extends from the dust sublimation radius (∼0.1 AU) up to about 1 AU (see also Espaillat et al. 2007, 2008). For typical infrared dust opacities, this model requires a minimum dust mass of $3 \times 10^{-5}\ M_\oplus$. Alternatively, the LkCa15's infrared SED can be fitted with an optically thin region that extends from 0.1 to 5 AU. In this case, the mass of dust would be $3 \times 10^{-6}\ M_\oplus$. The optically thin region and the optically thick disk would produce a 1.3 mm flux below 10^{-6} mJy and would therefore have a negligible effect on the overall disk millimeter emission. The same two models for the near-infrared emission can be applied to the case of the smooth viscous surface density profile. However in this case the outer disk is brighter in the mid-infrared than in the power-law case, and therefore the region emitting the infrared emission has to be smaller.

6. DISCUSSION

6.1. On the Origin of the Continuum Cavity

The results presented so far suggest at least two possible scenarios for the radial distribution of the circumstellar material around LkCa 15.

In the first case, most of the circumstellar dust is confined in a sharply truncated ring extending between 42 and 120 AU. Since no discontinuity is observed in the gas density at the edges of this dusty ring, this scenario requires a drop of the dust-to-gas ratio, or of the dust opacity, outside the ring. As discussed in Section 1, a sharp internal disk truncation can be the result of dynamical interactions with one, or more, giant planets (see, e.g., Bryden et al. 1999) or be due to the disk photoevaporation caused by the stellar radiation field (see, e.g., Gorti et al. 2009). This latter model suffer however two severe problems. First, it predicts a truncation in both the gaseous and dusty disk, which, as discussed in Section 5.1, it is not consistent with spatially resolved observations of the mm-wave CO emission. Second, it predicts that the accretion of material on the central star stops as soon as the cavity is opened, while the mass accretion rate measured toward LkCa 15 is about $\dot{M} = 3 \times 10^{-9}\ M_\odot\ \mathrm{yr}^{-1}$ (Hartmann et al. 1998).

Whether large (>20 AU) dust depleted cavities can be produced by the dynamical interaction with giant planets is still subject of debate. Zhu et al. (2011) showed that for large values of the viscosity parameter ($\alpha > 0.01$), a system with 3 or 4 Jupiter mass planets orbiting between 5 and 20 AU can lead to a largely depleted gap in the disk surface density. However, the mass accretion rate on the central star is predicted to drop below $5 \times 10^{-10}\ M_\odot\ \mathrm{yr}^{-1}$ in less that 1 Myr after the formation of the planets. Furthermore, a discontinuity in the gaseous disk surface density will not be consistent with the CO observations. Alternatively, a lower viscosity ($\alpha \leqslant 5 \times 10^{-3}$) would lead to larger values of $\dot{M}$ and less depleted cavities. While this

latter model might be consistent with the observation of the CO emission, it fails to explain the lack of mid-infrared dust continuum emission observed toward LkCa 15. To reconcile the measured values of $\dot{M}$ with the infrared SED in the framework of planet–disk interaction, Zhu et al. (2011) argue that low values of α have to be coupled with a decrease by at least one order of magnitude of the near- and mid-infrared dust optical depth in the region partially depleted by the planets. A drop of this magnitude in the dust opacity can be achieved through the coagulation of small, micron-sized grain into larger bodies. In the particular case of LkCa 15, we find that the dust opacity at 10 μm will decrease from about 3 cm^2 g^{-1} to 0.2 cm^2 g^{-1} by increasing the maximum grain size from the adopted value of 0.5 mm (Section 4) to 10 cm. It is therefore possible that the actual structure of the LkCa 15 inner disk is the result of an earlier phase characterized by the formation of large pebbles and boulders in the innermost disk regions (see, e.g., Brauer et al. 2008), followed by the formation of giant planets. If that happened in a low viscosity environment, the gas density within 40 AU would be high enough to explain both the measured mass accretion rate and the CO observations, and perhaps to allow the planetary cores to accrete the gas required to reach the Jupiter mass.

This scenario is compatible with the recent discovery of a possible protoplanet orbiting at about 16 AU from the central star discovered through aperture masking observations in the K' (∼2.1 μm) and L' (∼3.8 μm) bands (Kraus & Ireland 2012). The K' magnitude and $K'-L'$ color of the planet are consistent with a temperature of 1500 K and a mass of 6 M_J, or smaller. In addition the L' observations trace extended emission interpreted as evidence of circumplanetary material. However, following theoretical models for the planet disk interactions, this planet would be able to open only a relatively small gap in the dust distribution between 12 and 20 AU. To explain the cavity radius of 42 AU, at least another planet clearing the disk within 12 AU, and other two planets clearing the region between 20 and 42 AU would be required (see, e.g., Dodson-Robinson & Salyk 2011).

In an alternative scenario, which does not require multiple planets, the disk surface density is described by the smooth viscous model shown in Figure 3. In this case, the gas density decreases within 80 AU but it remains high enough to explain the small inner disk radius derived from the CO observations. This situation is similar to that proposed for MWC 758, where the ^{12}CO emission is centrally peaked while the dust emission traces a partially dust depleted disk within 70 AU from the central star (Isella et al. 2010b). It is important to note that the smooth best-fit model was derived in the assumption of constant dust opacity throughout the disk. By relaxing this assumption, we can interpret our results in terms of radial variation of the dust opacity, due, for example, to grain growth. Radial variations in the grain size distribution are indeed predicted by theoretical models for the dust evolution (Brauer et al. 2008) and can be observed by measuring radial variations of the mm-wave opacity slope β through spatially resolved multi-wavelengths observations of the dust emission (Isella et al. 2010a; Guilloteau et al. 2011). In the case of LkCa 15, the comparison of 1.3 and 3 mm observations suggests that β increases from 0.7–1.0 to 1.5–1.7 between 30 AU and 150 AU (Guilloteau et al. 2011). As shown in Figure 7, this variation would correspond to a decrease of the maximum grain size from about 8–30 to 0.3–3 mm, or to an increase of about a factor of two in the dust opacity at 1.3 mm. The observed variation in the grain size might therefore explain the observed cavity in the 1.3 mm dust emission without invoking multiple giant planets, but more sensitive observations at longer wavelengths are required to investigate the presence of large grains in the 1.3 mm continuum cavity.

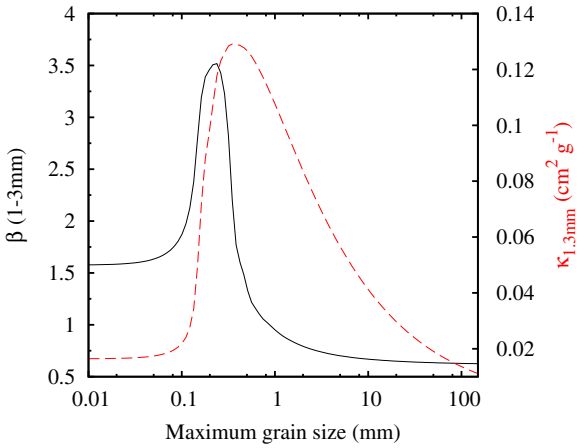

Figure 7. Dependence of the slope of the dust opacity β measured between 1.3 and 3 mm (solid curve) and of the dust opacity κ at 1.3 mm (dashed curve) on the maximum grain size, for a grain size distribution $n(a) \propto a^{-q}$, where $q = 3.5$ and the minimum grain size is 5×10^{-6} mm.

(A color version of this figure is available in the online journal.)

6.2. Investigating the Origin of Transition Disks with ALMA

Several experiments can be set up to investigate the origin of the inner cavities in transition disks by taking advantage of the superb imaging capabilities of the Atacama Large Millimeter Array (ALMA). Here we explore the possibility to use relatively low-angular-resolution observations, achievable during ALMA early science, to constrain the profile of the dust distribution at the edge of the dust continuum cavity. These observations can be used to disentangle the two possible scenarios discussed above. As shown in Figure 4, and discussed in Section 5.1, CARMA observations fail to distinguish between a sharp and smooth edge of the continuum cavity because they do not provide enough sensitivity on the spatial frequencies where the difference between the two models is the largest, namely between 100 and 700 kλ. On the other hand, Figure 8 shows that constraining the radial density profile at the edge of the continuum cavity is within the capabilities of ALMA in the early science phase. The leftmost panels of Figure 8 show the model of the dust emission corresponding to the best-fit solutions for the smooth viscous and power-law surface density profile discussed in Section 5.1. The maps in the rightmost panels represent ALMA band 9 (0.44 mm) simulated observations obtained using the array specifications for Cycle 0 observations and 30 minute on source integration. The structural differences between the two models are evident in these images: the smoothly varying $\Sigma(r)$ shows trace amounts of emission in the inner disk that is detectable with ALMA, while the inner region in the truncated disk model is devoid of emission and resolved. More quantitatively, Figure 9 shows the difference between the visibility profiles of the two different models as a function of the spatial frequency, where the colored region indicate the 3σ measurement uncertainties from the simulated observations. At the wavelength adopted for the simulation, the two models can be disentangled at high significance level on almost all spatial frequencies

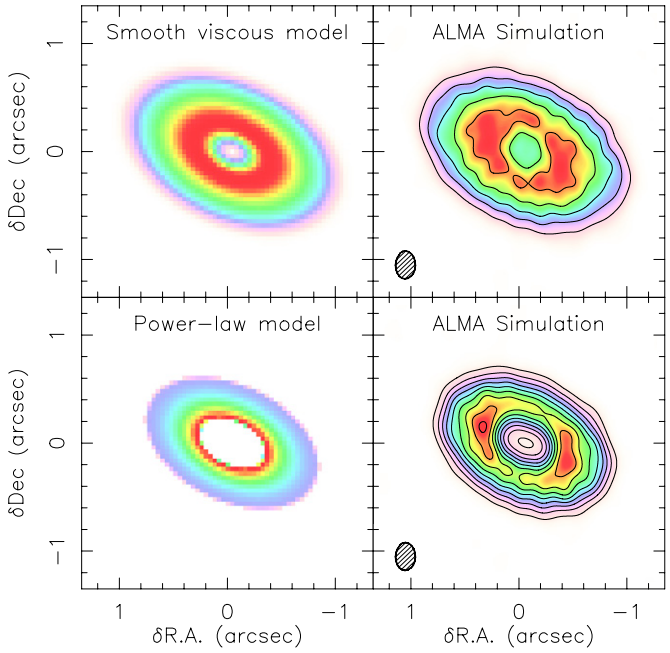

Figure 8. Simulated ALMA observations of 0.44 mm continuum emission corresponding to the smooth viscous (top panels) and power-law (bottom panels) best-fit models discussed in Section 5.1. The panels on the left show the model while the simulated observations are shown on the right column. The simulations assume a 30 minute on source integration and the default weather conditions for Band 9. ALMA will determine whether the inner edge of the disk is sharply truncated (possibly due to dynamical interactions with a planet) or varies smoothly with radius (possibly due to grain growth in the inner disk).

(A color version of this figure is available in the online journal.)

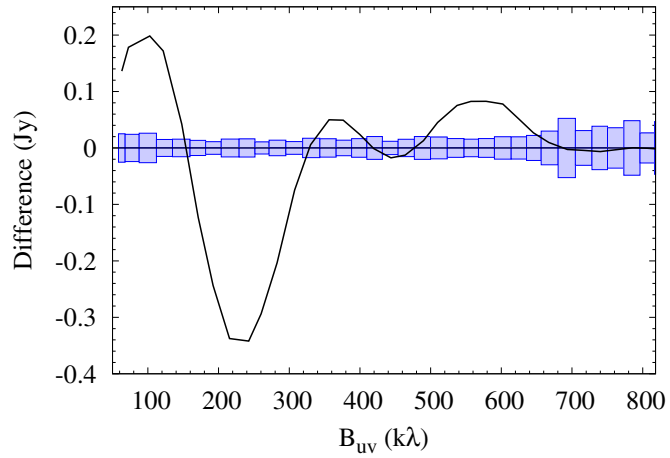

Figure 9. Difference in the visibility profile between the power-law and smooth viscous best-fit models (solid curve), compared to the 3σ sensitivity of ALMA early science observations at 0.44 mm (shaded region). This figure demonstrates that ALMA observations can reliably distinguish between two plausible geometries for transitions disks to identify the mechanism likely responsible for inner cavities.

(A color version of this figure is available in the online journal.)

shorter than 600 kλ, which correspond to baselines shorter than 270 m.

6.3. The LkCa 15 Outer Disk Structure

The discrepancy in the outer radius of the dusty and gaseous disk remains an unsolved issue since, as discussed in Section 5.1, it cannot be reconciled by adopting an exponentially tapered surface density profile. A caveat to this analysis is that our observations constrain the dust density only between 40 and 120 AU. The extrapolation of Σ to larger radii relies therefore on the assumption that the prescription of Equation (1) is valid across the all disk radial extent.

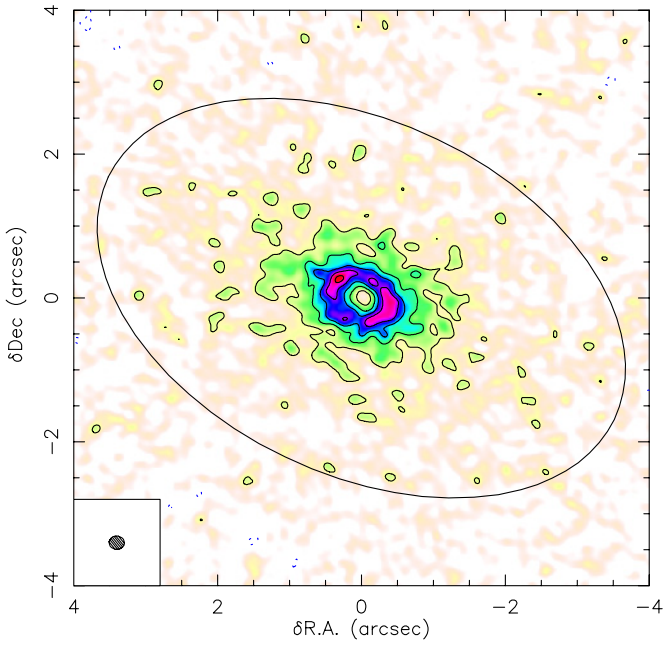

Figure 10. Simulated observations of the 1.3 mm dust continuum emission corresponding to the surface density profile derived from the analysis of the optically thin ^{13}CO line emission (Piétu et al. 2007). The simulations have been obtained by assuming the same *uv* coverage and noise level as in the CARMA observations. The image has been made by adopting uniform weighting to achieve a resolution of 0.″21 × 0.″19, as in panel (c) of Figure 1. Contours are plotted every 3σ, where the 1σ noise level is 0.43 mJy beam^{-1}.

(A color version of this figure is available in the online journal.)

To test this assumption we compare our results with the gas density inferred from the analysis of the ^{13}CO (1-0) emission by Piétu et al. (2007). In LkCa 15, the ^{13}CO (1-0) line is nearly optically thin and traces the density in the disk mid-plane. By comparing the observations to a power-law disk model, Piétu et al. (2007) find that the ^{13}CO surface density decreases as $r^{-3/2}$ from about 1.4×10^{16} cm^{-2} at 100 AU to 1.2×10^{15} cm^{-2} at 500 AU. If the ^{13}CO abundance is constant throughout the disk, then the decrease of the gas density is less steep than what is predicted by an exponentially tapered profile.

To check whether the disk surface density profile derived from CO observations is consistent with the dust continuum emission, we show in Figure 10 simulated CARMA observations of the 1.3 mm dust emission corresponding to a dust surface density $\Sigma_d(r) = 0.13 \times (r/100\,\mathrm{AU})^{-3/2}$ that extends between 42.5 AU and 550 AU. The surface density normalization is derived in order to reproduce the peak flux measured in our map. To facilitate the comparison with the observations, the simulated emission is observed at the same resolution and is affected by the same noise as in panel (c) of Figure 1.

We find that only the dust emission within about 200 AU would have been clearly detected while the flux arising from larger radii would have been lost in the noise. The limited sensitivity of the continuum observations seems therefore to be the major responsible for the different radial extent of the dust and gas emission. Nevertheless, the fact that the simulated emission is about 60% more extended than what is observed suggests that either the dust-to-gas ratio or the dust opacity decreases at about 130 AU from the central star.

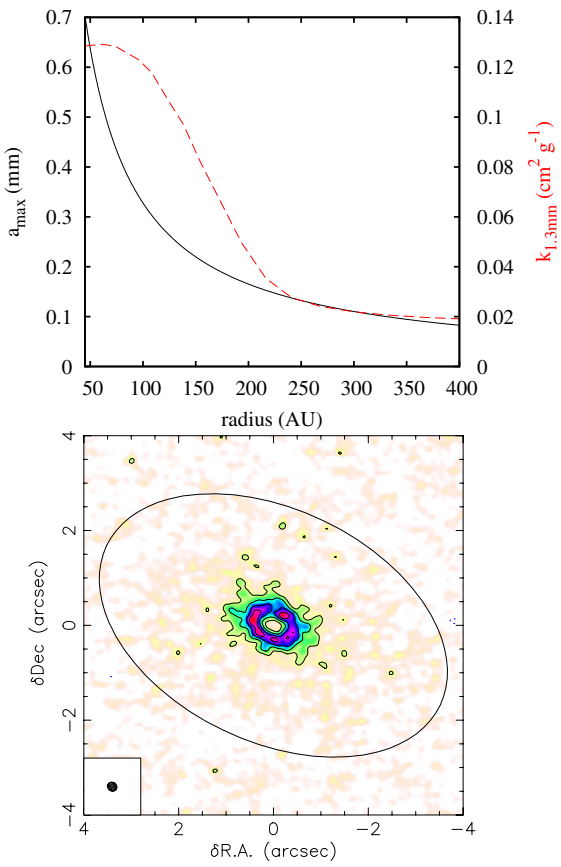

Figure 11. Top panel: dependence of the maximum grain size $a_{\rm max}$ (solid curve) and of the dust opacity κ at 1.3 mm (dashed curve) on the orbital radius, calculated assuming the grain growth model discussed in Section 6. Bottom panel: simulated observations of the 1.3 mm dust continuum emission corresponding to the surface density profile derived from the analysis of the optically thin ^{13}CO line emission (Piétu et al. 2007), accounting for the radial variation of the dust opacity due to grain growth. The decrease in the dust opacity between 100 and 200 AU results in a smaller effective radius for the dust continuum emission, compared to the case in which the dust opacity is constant throughout the disk (Figure 10).

(A color version of this figure is available in the online journal.)

In Section 6.1 we suggested that grain growth is required to explain the structure of the innermost disk regions independently from the presence of planets. Here we argue that grain growth might also provide a natural explanation for the smaller extent of the dust continuum emission. Grain growth models indeed predict that the outermost disk regions should be populated by sub-micron-sized grains, which have a 1.3 mm dust opacity almost a factor 10 smaller than the mean dust opacity adopted in our disk modeling (Figure 7). In the assumption that particles grow through mutual collisions and stick together by van der Walls forces, the maximum grain size $a_{\rm max}$ of the grain size distribution can be expressed as (Birnstiel et al. 2010)

$$a_{\rm max}(r) \simeq \frac{2\Sigma(r)}{\pi\alpha\rho_s}\frac{u_f^2}{c_s(r)^2}, \qquad (2)$$

where α is the viscosity parameter, u_f is the dust fragmentation velocity, Σ is the disk surface density, c_s is the sound speed, and ρ_s the dust density. Figure 11 shows the radial profile of $a_{\rm max}$, and of the corresponding dust opacity at 1.3 mm, calculated by assuming $\rho_s = 2$ g cm^2, $\alpha = 10^{-3}$, and $u_f = 1$ m s^{-1}. The surface density is that derived from the CO observations as discuss above, and the sound speed c_s is self-consistently calculated by assuming hydrostatic equilibrium (see Appendix E in Isella et al. 2009). Although the exact values of $a_{\rm max}$ depend on the assumptions on α and u_f, we find in general that a radial decrease of the maximum grain size corresponds to a drop in the 1.3 mm dust opacity. In particular, the decrease in $a_{\rm max}$ from 0.4 to 0.1 mm between 100 and 300 AU corresponds to a factor five decrease in the dust opacity. Given the sensitivity of our observations, the drop in the opacity would in practice lead to a smaller radius of the continuum emission, making the simulation much alike the observations (bottom panel of Figure 11).

This result suggests that the small disk radius measured in the dust continuum emission might be the result of a combined decrease in dust opacity due to radial variations in the grain size distribution and the finite sensitivity of our observations. Investigating this hypothesis requires high-angular-resolution multi-wavelength observations of the dust continuum emission.

7. SUMMARY

We report new CARMA 1.3 mm dust continuum observations toward LkCa 15 which resolve the disk on spatial scales of 30 AU. We find that 90% of the observed 1.3 mm dust emission arises from an azimuthally symmetric ring that contains about $5 \times 10^{-4}\,M_\odot$ of dust. The remaining 10% of the emission comes from a low-surface brightness tail that extends toward the northwest out to a radius of about 300 AU.

To investigate the origin of the inner cavity observed in the dust emission we constrain the radial profile of the dust density at the edge of the cavity and across the dusty ring. The comparison with theoretical disk models shows that the surface density is rather flat between 40 and 120 AU, and that the drop of dust emission is consistent with either a sharp truncation of the dusty disk at 42.5 AU, or with a smooth inward decreases of the dust density between 3 and 85 AU. Within 40 AU, the observations constrain the amount of dust between 10^{-6} and 7 $M_\oplus$, where the minimum and maximum limits are set by the near infrared SED modeling and by the millimeter-wave observations of the dust emission, respectively.

The recent discovery by Kraus & Ireland (2012) of a possible giant planet orbiting at 16 AU around LkCa 15 suggests that the dust distribution might be shaped by the dynamical clearing of this planet. However, at least three other Jupiter-size planets in addition to the one discovered by Kraus & Ireland would be required to explain a sharp truncation in the dusty disk at 42 AU (Zhu et al. 2011; Dodson-Robinson & Salyk 2011). In addition, the presence of planets should be coupled with low disk viscosity ($\alpha < 5 \times 10^{-3}$) and with a significant depletion of micron-size grains, to explain both the presence of gas within the dust depleted cavity and the lack of near- and mid-infrared emission (Zhu et al. 2011). Alternatively, our results are consistent with a smooth inward decrease in the dust opacity caused by the coagulation of small grains into larger bodies, as predicted by grain growth models. In this case, the dynamical clearing by the discovered planet would play a minor role in shaping the disk emission and no additional planets are necessary. We show that early science ALMA observations will be able to disentangle these two scenarios by constraining the slope of the dust density at the edge of the continuum cavity.

Finally, we find that 90% of the dust emission is confined within a radius of about 120 AU, while the gas emission is observed up to a radius of 900 AU. We find that this discrepancy cannot be reconciled using a exponentially tapered surface density profile but suggests a drop in the dust-to-gas ratio, or in the dust opacity, at radii larger than 120 AU. Using the grain growth model from Birnstiel et al. (2010), we show that a

Table 2
Date of the Observations and Source Coordinates

Date	Δt (yr)	R.A. (hh:mm:sec)	Decl. (deg:min:sec)
2007 Oct 27	7.816	04:39:17.799	22:21:03.289
2008 Dec 10	8.938	04:39:17.800	22:21:03.274
2010 Nov 26	10.898	04:39:17.801	22:21:03.247
2011 Jan 30	11.075	04:39:17.801	22:21:03.245

Notes. Column 1: date of the observations; Column 2: time baseline from year 2000; Columns 3 and 4: stellar coordinates at the epoch of the observation assuming a proper motion of $\mu_\alpha \cos\delta = 9.35$ mas yr^{-1} and $\mu_\delta = -13.55$ mas yr^{-1}.

decline in the maximum grain size with radius will reduce the dust opacity by a factor of five between 100 and 300 AU, with a corresponding decrease in the dust continuum emission.

Note added in proof. Since the work described in this paper was completed and submitted for publication, 850 μm observations of the dust continuum emission toward LkCa 15 that achieve a resolution of about 0.″25 have been published by Andrews et al. (2011a). These observations show that the continuum emission arises from a ring with the same properties of that discussed in this paper. In particular, they also find that the ring requires a rather flat surface density profile between about 40 and 120 AU.

We thank the OVRO/CARMA staff and the CARMA observers for their assistance in obtaining the data. Support for CARMA construction was derived from the Gordon and Betty Moore Foundation, the Kenneth T. and Eileen L. Norris Foundation, the James S. McDonnell Foundation, the Associates of the California Institute of Technology, the University of Chicago, the states of California, Illinois, and Maryland, and the National Science Foundation. Ongoing CARMA development and operations are supported by the National Science Foundation under a cooperative agreement, and by the CARMA partner universities. We acknowledge support from the Owens Valley Radio Observatory, which is supported by the National Science Foundation through grant AST 05-40399. This work was performed in part under contract with the Jet Propulsion Laboratory (JPL) funded by NASA through the Michelson Fellowship Program. JPL is managed for NASA by the California Institute of Technology. L.M.P. acknowledges support for graduate studies through a Fulbright-CONICYT scholarship.

APPENDIX

STELLAR PROPER MOTION

The proper motion for LkCa 15 has been measured by Roeeser et al. (2010) comparing *USNO-B1-0* (Monet et al. 2003) and Two Micron All Sky Survey data (Skrutskie et al. 2006), and by Zacharias et al. (2009; US Naval Observatory Twin Astrograph project). The first measurement leads to $\mu_\alpha \cos\delta = 9.1 \pm 2.1$ mas yr^{-1} and $\mu_\delta = -13.8 \pm 2.1$ mas yr^{-1}. The second to $\mu_\alpha \cos\delta = 9.6 \pm 2.2$ mas yr^{-1} and $\mu_\delta = -13.3 \pm 2.2$. The J2000 coordinates for epoch 2000 for LkCa 15 corrected for the proper motion are R.A. = 69.°824139 and Decl. = +22.°350945 (Roeeser et al. 2010), and R.A. = 69.°8241427 and Decl. = +22.°3509412 (Skrutskie et al. 2006). The difference between the two catalogs is about 13 mas, and is consistent with the quoted astrometric errors (i.e., 15 mas in both right ascension and declination in Roeeser et al. 2010, and 30 mas in Zacharias et al. 2009, respectively). Our CARMA observation have been corrected by assuming a mean proper motion of $\mu_\alpha \cos\delta = 9.35$ mas yr^{-1} and $\mu_\delta = -13.55$ mas yr^{-1}. The J2000 coordinates corrected for the proper motion at the epoch of the observations are listed in Table 2.

REFERENCES

Alexander, R. D., Clarke, C. J., & Pringle, J. E. 2006a, MNRAS, 369, 216
Alexander, R. D., Clarke, C. J., & Pringle, J. E. 2006b, MNRAS, 369, 229
Andrews, S. M., Rosenfeld, K. A., Wilner, D. J., & Bremer, M. 2011a, ApJ, 742, L5
Andrews, S. M., & Williams, J. P. 2005, ApJ, 631, 1134
Andrews, S. M., & Williams, J. P. 2007, ApJ, 671, 1800
Andrews, S. M., Wilner, D. J., Espaillat, C., et al. 2011b, ApJ, 732, 42
Birnstiel, T., Ricci, L., Trotta, F., et al. 2010, A&A, 516, L14
Brauer, F., Dullemond, C. P., & Henning, T. 2008, A&A, 480, 859
Brown, J. M., Blake, G. A., Qi, C., et al. 2009, ApJ, 704, 496
Bryden, G., Chen, X., Lin, D. N. C., Nelson, R. P., & Papaloizou, J. C. B. 1999, ApJ, 514, 344
Calvet, N., D'Alessio, P., Watson, D. M., et al. 2005, ApJ, 630, L185
Chapillon, E., Guilloteau, S., Dutrey, A., & Piétu, V. 2008, A&A, 488, 565
Chiang, E. I., & Goldreich, P. 1997, ApJ, 490, 368
Dodson-Robinson, S. E., & Salyk, C. 2011, ApJ, 738, 131
Dullemond, C. P., & Dominik, C. 2005, A&A, 434, 971
Dullemond, C. P., Dominik, C., & Natta, A. 2001, ApJ, 560, 957
Dutrey, A., Guilloteau, S., Duvert, G., et al. 1996, A&A, 309, 493
Espaillat, C., Calvet, N., D'Alessio, P., et al. 2007, ApJ, 670, L135
Espaillat, C., Calvet, N., Luhman, K. L., Muzerolle, J., & D'Alessio, P. 2008, ApJ, 682, L125
Gorti, U., Dullemond, C. P., & Hollenbach, D. 2009, ApJ, 705, 1237
Guilloteau, S., Dutrey, A., Piétu, V., & Boehler, Y. 2011, A&A, 529, A105
Hartmann, L., Calvet, N., Gullbring, E., & D'Alessio, P. 1998, ApJ, 495, 385
Hartmann, L., Megeath, S. T., Allen, L., et al. 2005, ApJ, 629, 881
Hughes, A. M., Andrews, S. M., Espaillat, C., et al. 2009, ApJ, 698, 131
Hughes, A. M., Wilner, D. J., Qi, C., & Hogerheijde, M. R. 2008, ApJ, 678, 1119
Isella, A., Carpenter, J. M., & Sargent, A. I. 2009, ApJ, 701, 260
Isella, A., Carpenter, J. M., & Sargent, A. I. 2010a, ApJ, 714, 1746
Isella, A., Natta, A., Wilner, D., Carpenter, J. M., & Testi, L. 2010b, ApJ, 725, 1735
Isella, A., Testi, L., Natta, A., et al. 2007, A&A, 469, 213
Kenyon, S. J., & Hartmann, L. 1995, ApJS, 101, 117
Kitamura, Y., Momose, M., Yokogawa, S., et al. 2002, ApJ, 581, 357
Kraus, A. L., & Ireland, M. J. 2012, ApJ, 745, 5
Lynden-Bell, D., & Pringle, J. E. 1974, MNRAS, 168, 603
Monet, D. G., Levine, S. E., Canzian, B., et al. 2003, AJ, 125, 984
Mulders, G. D., Dominik, C., & Min, M. 2010, A&A, 512, A11
Öberg, K. I., Qi, C., Fogel, J. K. J., et al. 2010, ApJ, 720, 480
Owen, J. E., Ercolano, B., Clarke, C. J., & Alexander, R. D. 2010, MNRAS, 401, 1415
Piétu, V., Dutrey, A., & Guilloteau, S. 2007, A&A, 467, 163
Piétu, V., Dutrey, A., Guilloteau, S., Chapillon, E., & Pety, J. 2006, A&A, 460, L43
Piétu, V., Guilloteau, S., & Dutrey, A. 2005, A&A, 443, 945
Pollack, J. B., Hollenbach, D., Beckwith, S., et al. 1994, ApJ, 421, 615
Rebull, L. M., Padgett, D. L., McCabe, C.-E., et al. 2010, ApJS, 186, 259
Rodmann, J., Henning, T., Chandler, C. J., Mundy, L. G., & Wilner, D. J. 2006, A&A, 446, 211
Roeeser, S., Demleitner, M., & Schilbach, E. 2010, VizieR Online Data Catalog, 1317, 0
Shakura, N. I., & Sunyaev, R. A. 1973, A&A, 24, 337
Simon, M., Dutrey, A., & Guilloteau, S. 2000, ApJ, 545, 1034
Skrutskie, M. F., Cutri, R. M., Stiening, R., et al. 2006, AJ, 131, 1163
Tanaka, H., Himeno, Y., & Ida, S. 2005, ApJ, 625, 414
Thalmann, C., Grady, C. A., Goto, M., et al. 2010, ApJ, 718, L87
Thompson, A. R., Moran, J. M., & Swenson, G. W. (ed.) 1991, in Interferometry and Synthesis in Radio Astronomy, (Malabar, FL: Krieger),
van den Ancker, M. E., de Winter, D., & Tjin A Djie, H. R. E. 1998, A&A, 330, 145
Zacharias, N., Finch, C., Girard, T., et al. 2009, VizieR Online Data Catalog, 1315, 0
Zhu, Z., Nelson, R. P., Hartmann, L., Espaillat, C., & Calvet, N. 2011, ApJ, 729, 47